Characterization of nuclear break-up as a function of hard-scattering kinematics using dijets in p+Pb collisions at $\sqrt{s_{\mathrm{NN}}}$=8.16 TeV with the ATLAS detector

The ATLAS Collaboration

This note presents the first study of the sensitivity of event geometry estimators to the initial state kinematics of the hard scattering in proton-lead collisions. The data used in the analysis were recorded by the ATLAS detector at a center-of-mass energy of 8.16 TeV and correspond to a luminosity of 56 nb^{-1}. This analysis uses dijets as proxies for the kinematics of the initial state parton-parton scattering and correlates it with the energy deposited in the Zero Degree Calorimeter and the transverse energy recorded in the Forward Calorimeter.

1 Introduction

Results obtained from the analysis of hard processes in proton-lead (p+Pb) data collected by LHC experiments have contributed to the differentiation between hot and cold nuclear matter effects. The modifications of parton distribution functions (PDFs) in the nuclear environment [1] have been addressed by measurements in several channels, such as W bosons [2] by CMS, Z bosons [3] by ATLAS, dijets in p+Pb collisions at 5.02 TeV by CMS [4], and dijets in ultra-peripheral Pb+Pb collisions (UPCs) by ATLAS [5]. ATLAS [6] and CMS [7] have also measured $t\bar{t}$ production in p+Pb at 8.16 TeV, providing additional data to constrain nuclear PDF (nPDF) parameterizations. The LHCb collaboration analyzed prompt D^0 meson production in p+Pb collisions at 5.02 TeV [8], providing data to constrain nPDFs at lower Q^2 and parton momentum fractions compared to the measurements listed above. ATLAS also measured forward dijet azimuthal correlations and conditional yields in 5.02 TeV p+Pb collisions, to search for evidence of high-density gluon states [9].

Hard process rates in proton-nucleus (p+A) collisions are also analyzed under different event selections sensitive to the collision geometry by using detector quantities expected to scale with the number of binary collisions. ATLAS observed an event activity bias in the first measurement of inclusive jet production in p+Pb at 5.02 TeV using Run 1 data [10]. The analysis reported a significant suppression of the jet production in central events compared to peripheral events, with centrality defined using the transverse energy measured in the Forward Calorimeter (FCal). The suppression was found to be a function of only the total jet energy. A similar observation was made by PHENIX at RHIC [11]. These results were interpreted as evidence that protons in a configuration containing a parton with large x have a significantly smaller than average cross-section and size when interacting with a nuclear target [12], a manifestation of so-called color fluctuation (CF) effects [13–15]. Recently, ATLAS analyzed the centrality dependence of dijet production in p+Pb data collected at 8.16 TeV [16]. This result is also consistent with the CF interpretation proposed in [12]. The measurement showed how the event activity bias in p+Pb is driven by the initial state kinematics of the hard-scatter parton in the proton, providing unprecedented input to characterize CF effects in p+A collisions.

p+A collisions are also used to search for signatures of jet quenching effects in small systems. For these studies, it is of interest to analyze the most central collisions by using robust and unambiguous selections, not sensitive to CF effects [17]. As an alternative way to select different geometries in p+A events, one can classify events based on the number of spectator neutrons measured in the nucleus-going Zero-Degree Calorimeter (ZDC). ALICE [18] and ATLAS [19] have used the ZDC as a way to search for energy loss signatures in central events, arguing that this selection is less biased than the multiplicity-based selection method. However, the dynamics of the nuclear breakup in p+Pb collisions remain largely unknown and are poorly modeled by event generators, especially in the presence of a hard-scattering. The only measurement of forward neutrons in p+Pb, published by ALICE in 2022 [20], reported the energy accumulated in the neutron ZDC on both sides as a function of the estimated number of binary collisions. The results, self-normalized to the average in minimum bias (MB) events in p+Pb collisions, found the energy in the Pb-going neutron ZDC to monotonically increase with number of binary collisions, showing correlation between these two quantities.

Recently, the authors of [21] argued that CF effects may also be relevant in the nuclear breakup process in UPCs characterized by a resolved photon exchange. The proposed model links the number of nucleons wounded by interactions with a vector meson with the nuclear breakup dynamics, suggesting that studying forward neutron production can provide a direct handle on the number of binary collisions. Such effects, related to the number of wounded nucleons, can also change the understanding of ZDC energy measured in

e^-+A collisions at the future Electron-Ion Collider, where it has been proposed as a possible centrality tag [22]. A similar model, using a proton instead of a vector meson in the scattering with the nucleus, can be used for the nuclear breakup in p+Pb interactions. Given the dependence of CF effects on the hard-scattering in p+Pb collisions, it is of great interest to study the correlation between the kinematics of the hard-scattered partons, the neutron energy at zero degrees after nuclear breakup and the forward calorimeter event activity in these events.

This analysis presents the first characterization of very forward energy in dijet events in p+Pb collisions at LHC energies, using 56 nb^{-1} of 8.16 TeV p+Pb data collected by ATLAS during 2016. The energy deposited in the ZDC and the transverse energy recorded in the FCal, both measured on the Pb-going side, were measured as a function of the Bjorken-x of the proton, estimated with reconstructed dijet kinematics. The correlation between the transverse energy measured in the FCal, FCal $\sum E_{\mathrm{T}}^{\mathrm{Pb}}$, and the energy deposited in the ZDC, $E_{\mathrm{ZDC}}^{\mathrm{Pb}}$, is also investigated.

Following [16], dijets are defined using the two highest transverse momentum jets in a given collision, measured over a wide range of transverse momentum, p_{T}, and center-of-mass (CM) rapidity, y^{CM}, to access a broad x_p phase space. x_p is estimated using the final-state kinematics of the two highest p_{T} jets in each event by using

$$x_p = \frac{p_{\mathrm{T},1} e^{y_1^{\mathrm{CM}}} + p_{\mathrm{T},2} e^{y_2^{\mathrm{CM}}}}{\sqrt{s_{\mathrm{NN}}}}, \tag{1}$$

where $p_{\mathrm{T},1}$ ($p_{\mathrm{T},2}$) and y_1^{CM} (y_2^{CM}) denote the transverse momentum and the rapidity of the leading (sub-leading) jet. The quantity $\sqrt{s_{\mathrm{NN}}}$ is the nucleon-nucleon center-of-mass energy of the p+Pb collision system, 8.16 TeV. In simulation, this estimate based on final-state jet kinematics was found to be 6-8% below the parton-level x_p, on average, for the kinematics considered here.

In this analysis, x_p is unfolded for experimental effects due to the finite precision of jet reconstruction, and measured at the generator level. $E_{\mathrm{ZDC}}^{\mathrm{Pb}}$ and FCal $\sum E_{\mathrm{T}}^{\mathrm{Pb}}$ are not unfolded for experimental effects, as was done when used for centrality selections in previous analyses [10, 16, 19].

The normalized $E_{\mathrm{ZDC}}^{\mathrm{Pb}}$ and FCal $\sum E_{\mathrm{T}}^{\mathrm{Pb}}$ distributions are measured in each of the x_p bins defined for the analysis. The means of the distributions, $\langle E_{\mathrm{ZDC}}^{\mathrm{Pb}} \rangle$ and $\langle$FCal $\sum E_{\mathrm{T}}^{\mathrm{Pb}} \rangle$, are reported as a function of x_p, to characterize the evolution of forward energy flow as a function of the change in proton configuration, accessed via x_p.

Additionally, for the first time, the correlation between $E_{\mathrm{ZDC}}^{\mathrm{Pb}}$ and FCal $\sum E_{\mathrm{T}}^{\mathrm{Pb}}$ is also analyzed, to provide insights about the underlying physics linking event activity and nuclear breakup dynamics in p+Pb collisions. This data represents a novel approach to study geometry in proton-nucleus collisions and provides new insights into the role of proton configurations in the dynamics characterizing these reactions.

2 ATLAS detector

The measurement presented in this paper is performed using the ATLAS[1] calorimeter, inner detector, trigger, and data acquisition systems [23]. An extensive software suite [24] is used in the reconstruction

---

[1] ATLAS uses a right-handed coordinate system with its origin at the nominal interaction point (IP) in the center of the detector and the z-axis along the beam pipe. The x-axis points from the IP to the center of the LHC ring, and the y-axis points upwards. Cylindrical coordinates (ρ,ϕ) are used in the transverse plane, ϕ being the azimuthal angle around the z-axis. The psuedorapidity is defined in terms of the polar angle θ as $\eta = -\ln \tan(\theta/2)$. Angular distance is measured in units of $\Delta R \equiv \sqrt{(\Delta\eta)^2 + (\Delta\phi)^2}$.

and analysis of real and simulated data, in detector operations, and in the trigger and data acquisition systems of the experiment.

The calorimeter system consists of a sampling liquid-argon (LAr) electromagnetic (EM) calorimeter covering $|\eta| < 3.2$, a steel-scintillator sampling hadronic calorimeter covering $|\eta| < 1.7$, LAr hadronic calorimeters covering $1.5 < |\eta| < 3.2$, and two LAr FCal covering $3.2 < |\eta| < 4.9$. The EM calorimeters are segmented longitudinally in shower depth into three layers with an additional presampler layer covering $|\eta| < 1.8$. The hadronic calorimeters have three sampling layers longitudinal in shower depth for $|\eta| < 1.7$ and four sampling layers for $1.5 < |\eta| < 3.2$. During the 2016 p+Pb data taking, a sector of the hadronic endcap calorimeter (HEC), corresponding to $1.5 < \eta < 3.2$ and $-\pi < \phi < -\pi/2$ was disabled.

The inner detector measures charged particles within the pseudorapidity interval $|\eta| < 2.5$ using a combination of silicon pixel detectors, silicon microstrip detectors (SCT), and a straw-tube transition radiation tracker (TRT), all immersed in a 2 T axial magnetic field [23]. Each of the three detectors is composed of a barrel and two symmetric endcap sections. The pixel detector is composed of four layers including the insertable B-layer [25, 26]. The SCT barrel section contains four layers of modules with sensors on both sides, and each endcap consists of nine layers of double-sided modules with radial strips. The TRT contains layers of staggered straws interleaved with the transition radiation material.

The ATLAS ZDC consists of two detectors located in absorbers ±140 m from the ATLAS interaction point. Each detector is a sampling calorimiter made up of four modules each with a material budget of 1.14 hadronic interaction lengths. The modules are made of layers of tungsten plates with quartz rods interspersed between. They measure forward-going neutral particles with $|\eta| > 8.3$, primarily neutrons from nuclear breakup, which carry the original per-nucleon beam energy up to an additional smearing from nuclear Fermi momentum, and very forward neutral particles produced in the interaction.

ATLAS uses a two-level trigger system. The first-level trigger (Level 1) is hardware-based and implemented with custom electronics. It is followed by the software-based high-level trigger (HLT) [27].

3 Data selection and Monte Carlo Simulations

For the 2016 p+Pb run at $\sqrt{s_{\mathrm{NN}}}$ = 8.16 TeV, the LHC beam energy configuration was asymmetric between the protons (6.5 TeV), and the Pb nuclei (2.56 TeV/nucleon), resulting in a rapidity shift of the center of mass by 0.465 units toward the proton-going direction. The data were collected over two running periods characterized by opposite beam directions. In the first period of the data-taking, when Pb ions circulated clockwise in the LHC, a total integrated luminosity of 56 nb^{-1} was collected. The data analyzed in this note are comprised solely of the first data-taking period, referred to as the p+Pb orientation. The second data-taking period is not used in this analysis since the presence of a detector from the LHCf experiment [28] precluded a precise measurement of the neutron energy flow. The positive η direction used in the analysis is defined by the p-going direction.

The p+Pb data at $\sqrt{s_{\mathrm{NN}}}$ = 8.16 TeV used in this analysis were required to satisfy detector and data-quality requirements, as well as to contain at least one reconstructed primary vertex and two reconstructed jets. A set of fully efficient central and forward single-jet triggers [27], characterized by different p_{T} thresholds, were chosen to provide full p_{T} coverage over a wide pseudorapidity range, corresponding to $-3.1 < \eta < 4.5$.

In this analysis, jets with $R = 0.4$ were formed from calorimeter towers. The leading (sub-leading) jet was required to have $p_T > 40$ (30) GeV. Events with either the leading or the sub-leading jet reconstructed in the acceptance of the disabled HEC region were discarded in both data and MC. In order to define a rejection criterion for the analysis, the disabled region was increased by an additional 0.4 margin in both pseudorapidity and azimuthal angle, as done in previous jet analyses using these datasets [16]. In this way, jets with constituents affected by the disabled HEC are not considered.

The centrality of the p+Pb events is defined using the total transverse energy in the Pb-going FCal, ΣE_T^{Pb} [29, 30], and is used in the analysis in order to effectively reject contributions to the jet production from UPCs. This background was quantified through a study which used rapidity gap selections and was found to have a negligible contribution to the 0–90% centrality interval used in this analysis. The leading and sub-leading jets were required to be at least 0.4 pseudorapidity units away from the Pb-going FCal to reject events where the centrality-determining detector is directly biased by the contribution from a jet. All these selections are consistent with the p+Pb analysis presented in [16].

In-time pile-up events are rejected by requiring that no secondary vertices have more than 6 associated tracks. This removes approximately 11.9% of events from the sample.

This analysis used Monte Carlo (MC) simulations to evaluate the performance of the detector and analysis procedure, and to correct the measured distributions for detector effects. The detector response in all MC samples was simulated using Geant4 [31, 32]. The disabled HEC sector is replicated in the simulation. The p+Pb MC sample makes use of dijet events from 8.16 TeV pp collisions, including the boost in rapidity with respect to the lab frame that is in the data, simulated by Pythia8 [33] with the A14 set of tuned parameters [34] and the NNPDF2.3LO parton distribution functions [35]. Events from the Pythia8 dijet sample were overlaid with events from a dedicated p+Pb data sample collected using MB triggers. The overlay procedure combines the Pythia8 and data events during the digitization step of simulation. An event-by-event reweighting procedure was applied to the MC overlay sample, such that the resulting FCal $\sum E_T^{Pb}$ distribution better matches that of the dijet data sample.

4 Analysis

The FCal is comprised of calorimeter towers covering the region $3.2 < |\eta| < 4.9$, segmented with fine granularity in η and ϕ. The EM energy scale is used to measure the energy in each tower (E_{tower}^{EM}) [36]. The EM scale properly corrects the energy deposited by photons and electrons, but does not include any compensation to correct for the differences between EM and hadronic showers. The total transverse energy in the Pb-going FCal, FCal $\sum E_T^{Pb}$, is defined by a sum over the projection of each E_{tower}^{EM} into the transverse plane, for the towers in the pseudorapiditiy hemisphere facing the Pb ion. This definition of FCal $\sum E_T^{Pb}$ is consistent with the characterization of centrality used in previous ATLAS p+Pb analyses, for example in [16].

In a typical p+Pb event involving a hard scattering, most of the energy deposited into the Pb-going ZDC originates from spectator neutrons evaporating off the nucleus. A peaked structure arises in the low region of the ZDC energy spectrum due to the response to small number of neutrons. An example of the ZDC energy spectrum and peak fitting procedure is displayed in Figure 1. The first peak in this structure represents the ZDC response to the energy of a single spectator neutron. The absolute energy response of the ZDC modules is calibrated by a Lagrangian optimization procedure that sets the mean of the single neutron peak equal to the nominal per nucleon beam energy and adjusts calibration factors to minimize the
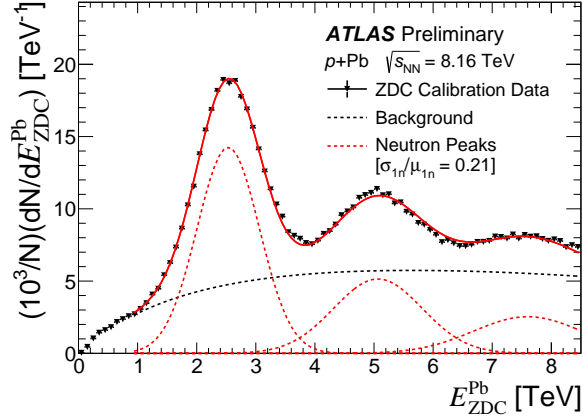
Figure 1: Low energy region of the post-calibration ZDC spectrum for events in the ZDC calibration stream. All the fit components are displayed using dashed lines. The fit result is shown by the solid red line.

width of the single neutron peak. The calibration procedure is performed throughout the run to account for changes in the detector response arising across the data taking. Following calibration, a simultaneous fit is performed to the first three neutron peaks, as well as a background term. These fits are used to validate the energy scale set by the calibration. The functional form of the background term was chosen to facilitate fit convergence in the 1–3 neutron range, but it is not expected to physically model the relative contributions between 1n–3n events. The fit procedure is applied on a per-run basis, to account for changes in the detector response during data-taking.

The spread on the single neutron peak originates from two separate sources. Firstly, the ZDC is a sampling calorimeter that has a finite experimental resolution. Secondly, the contribution from nuclear Fermi momentum smears the neutron energy away from the nominal per-nucleon beam energy. The use of a Gaussian to model the calorimeter response to a single neutron is motivated by the assumption that the modification from the convolution of these two sources is roughly symmetric. Below 1 TeV the detector is primarily observing a mix of low-energy photons and beam backgrounds, with a negligible fraction from single neutrons. The ZDC amplitude reconstruction procedure also requires pulse heights well above detector noise that limit its precision below 1 TeV. Therefore, below that threshold, the measured energy is treated as zero.

The $E_{\mathrm{ZDC}}^{\mathrm{Pb}}$ distribution after the in-time pile-up rejection displays an elbow in the large $E_{\mathrm{ZDC}}^{\mathrm{Pb}}$ tail indicative of residual pile-up. This residual pile-up is not seen in the FCal $\sum E_{\mathrm{T}}^{\mathrm{Pb}}$ spectrum, indicating that these backgrounds come from interactions that either only produce particles at very far forward rapidities or happen away from the IP. To correct the $E_{\mathrm{ZDC}}^{\mathrm{Pb}}$ spectrum in each x_p bin, a template fit and subtraction is performed. This removes approximately 0.19% of events from the sample.

Similarly to previous ATLAS jet measurements in p+Pb [16, 19] and Pb+Pb [37] collisions, the jets used in this analysis were reconstructed using the anti-k_t algorithm [38]. The jet reconstruction performance was characterized by evaluating the jet energy scale (JES) and resolution (JER), which correspond to the mean and variance of the $p_{\mathrm{T}}^{\mathrm{reco}}/p_{\mathrm{T}}^{\mathrm{gen}}$ distributions, where $p_{\mathrm{T}}^{\mathrm{gen}}$ denotes the transverse momentum of the matched generator-level jet in simulation. The jet reconstruction efficiency for jets with $p_{\mathrm{T}}^{\mathrm{reco}} > 5$ GeV was also studied using MC simulations and found to be greater than 99% in all η regions considered for the analysis for $p_{\mathrm{T}}^{\mathrm{gen}} > 25$ GeV. The JES and the JER for this data sample were scrutinized in detail in a

previous analysis, see [16] for all the relevant details. All the JES and JER-related effects were taken into account by the unfolding procedure discussed below.

This analysis considered events where the two highest p_T jets have reconstructed $p_{T,1} > 40$ GeV, $p_{T,2} > 30$ GeV and $-2.8 < \eta_1, \eta_2 < 4.5$. The asymmetric η requirement was imposed to avoid jets biasing the centrality determination in the Pb-going FCal.

To correct for detector effects and bin migration due to finite jet energy resolution, dijet events were unfolded in x_p using a two-dimensional Bayesian procedure [39], implemented within the RooUnfold package [40]. FCal $\sum E_T^{Pb}$ and E_{ZDC}^{Pb} were propagated through the unfolding procedure with fully diagonal migration matrices, preserving the event-level correlation between the hard-scattering kinematics and each of the calorimetric energies.

An efficiency correction was included in the unfolding to account for reconstructed jets that migrate out of the measurement phase space at the detector-level due to energy resolution effects, as well as to the disabled HEC region.

Each response matrix was reweighted at the event level by the ratio of reconstructed data to reconstructed MC simulation, as a function of x_p, such that the MC spectrum better matches the shape of the data. The statistical uncertainties in the resulting FCal $\sum E_T^{Pb}$ and the E_{ZDC}^{Pb} distributions, binned as a function of x_p, were evaluated using a bootstrapping method [41].

5 Systematic uncertainties

This measurement unfolds experimental effects on the dijets to access x_p at the generator level . This approach is subject to systematic uncertainties associated with the JES and JER, the unfolding procedure, and a systematic uncertainty due to a sector of the HEC being disabled for the running period. Other sources of systematic uncertainty, such as those related to the removal of the residual pile-up in the ZDC, were found to be negligible. For each source of systematic uncertainty, except for the uncertainty on the disabled HEC sector, the entire analysis is repeated by varying the response matrix according to the systematic variation. The difference between the nominal measurement and that obtained with the systematic variation is taken as the systematic uncertainty.

The JES uncertainty for this analysis has three components. The first was evaluated using *in situ* studies of the calorimeter response of jets reconstructed with the procedure used in 13 TeV pp collisions [42]. The second component accounts for the relative energy scale difference between the jet reconstruction procedures used in this analysis and those in 13 TeV pp collisions [43]. The third JES component accounts for potential inaccuracies in the MC sample's description of the relative abundances of jets initiated by quarks and gluons and of the calorimetric response to quark and gluon jets. To account for the uncertainty on the JES in the dijet measurement, each component was varied separately by ±1 standard deviation in the MC sample, applied as a function of p_T and η, and the response matrices were recomputed. The data were then unfolded with the modified matrices.

To evaluate the uncertainty associated with the JER, the p_T of reconstructed jets in the MC sample is smeared using a Gaussian to match the JER observed in data, producing modified response matrices. The smearing factor was taken from *in situ* studies of dijet energy balance [42]. An additional uncertainty was included to account for differences between the tower-based jet reconstruction and the jet reconstruction used in the analysis of 13 TeV pp data, as well as differences in calibration procedures [43].

The systematic uncertainty on the unfolding procedure is related to the sensitivity to the choice of the prior distribution. To determine the sensitivity of the results to the reweighting procedure, a new set of response matrices was generated without reweighting at the event level, and the full analysis procedure was repeated.

Events with a leading or sub-leading reconstructed level jet that falls within $|\Delta\eta| < 0.4$ or $|\Delta\phi| < 0.4$ of the region covered by the disabled HEC sector have been removed from the analysis. The systematic uncertainty associated with this removal was evaluated by increasing the exclusion region by 0.1 in both azimuth and pseudorapidity, and repeating the analysis procedure. The difference between the nominal exclusion and increased exclusion was taken as a systematic uncertainty and is symmetrized.

The variations for each systematic uncertainty were then added in quadrature to produce the total systematic uncertainties on each data point. The total systematic uncertainties on the normalized $E_{\text{ZDC}}^{\text{Pb}}$ and FCal $\sum E_{\text{T}}^{\text{Pb}}$ distributions are shown, for two representative x_p bins of the measurement, in Figures 2 and 3, respectively.
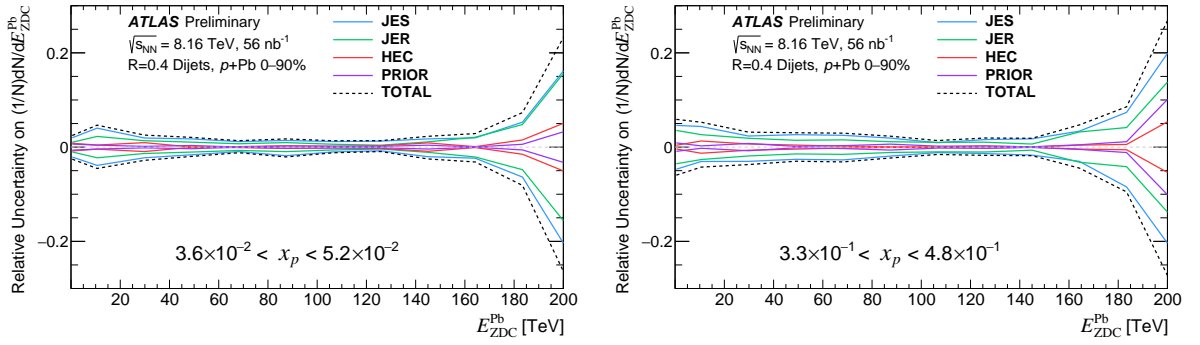

Figure 2: Relative systematic uncertainties on normalized $E_{\text{ZDC}}^{\text{Pb}}$ in selected bins of x_p. Each panel shows the total systematic uncertainty (black dashed line), as well as the contributions from each source, namely the JES, JER, unfolding PRIOR, and disabled HEC sector exclusion.
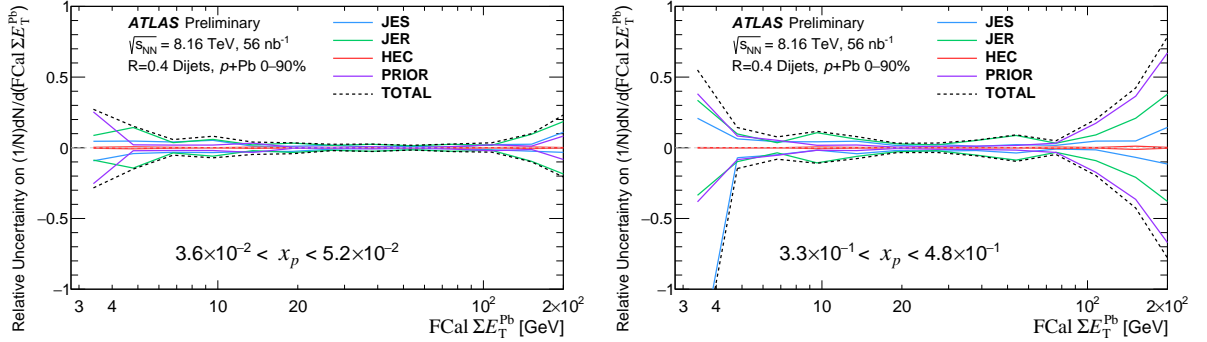

Figure 3: Relative systematic uncertainties on normalized FCal $\sum E_{\text{T}}^{\text{Pb}}$ in selected bins of x_p. Each panel shows the total systematic uncertainty (black dashed line), as well as the contributions from each source, namely the JES, JER, unfolding PRIOR, and disabled HEC sector exclusion.

The $E_{\text{ZDC}}^{\text{Pb}}$ systematic uncertainty is dominated by the JES and the JER, but are within 10% for all but the largest $E_{\text{ZDC}}^{\text{Pb}}$ bins. The systematic uncertainty on the FCal $\sum E_{\text{T}}^{\text{Pb}}$ distributions is dominated by contributions
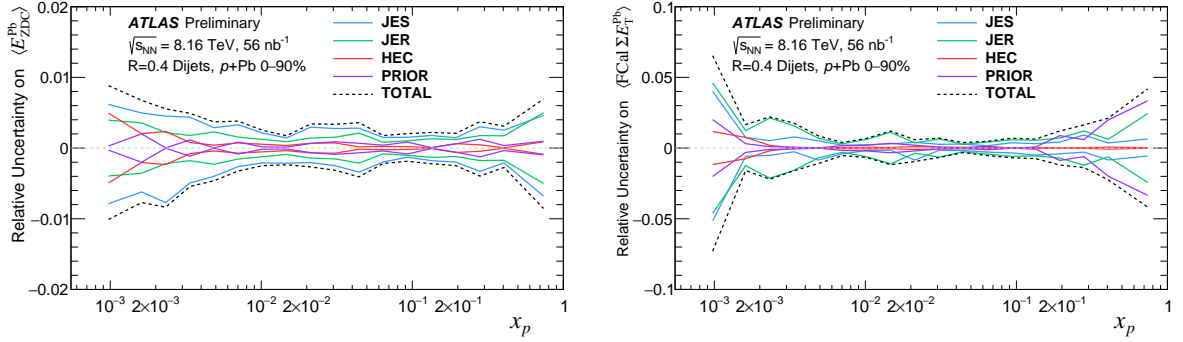
Figure 4: Relative systematic uncertainties on $\langle E_{\mathrm{ZDC}}^{\mathrm{Pb}} \rangle$ (left) and $\langle \mathrm{FCal} \sum E_{\mathrm{T}}^{\mathrm{Pb}} \rangle$ (right) as a function of x_p. Each panel shows the total systematic uncertainty (black dashed line), as well as the contributions from each source, namely the JES, JER, unfolding PRIOR, and disabled HEC sector exclusion.

from the JES, JER, and prior components. The uncertainties are relatively modest in the middle of the FCal $\sum E_{\mathrm{T}}^{\mathrm{Pb}}$ distribution, but increase at high FCal $\sum E_{\mathrm{T}}^{\mathrm{Pb}}$ where the dijet yield decreases dramatically. The sensitivity of the measurement to the choice of prior is especially large (up to 3%) in high-x_p bins, where the differences between the FCal $\sum E_{\mathrm{T}}^{\mathrm{Pb}}$ distributions in the MC sample and the data is largest.

The total systematic uncertainty on the distributions of $\langle E_{\mathrm{ZDC}}^{\mathrm{Pb}} \rangle$ and $\langle \mathrm{FCal} \sum E_{\mathrm{T}}^{\mathrm{Pb}} \rangle$ are displayed in Figure 4. The $\langle E_{\mathrm{ZDC}}^{\mathrm{Pb}} \rangle$ and $\langle \mathrm{FCal} \sum E_{\mathrm{T}}^{\mathrm{Pb}} \rangle$ uncertainty is below 1% in all of the x_p coverage. In this analysis, when ratios are constructed, the JES, JER and HEC uncertainties are considered correlated, while the prior uncertainty is treated as uncorrelated.

6 Results

6.1 Measurement of $E_{\text{ZDC}}^{\text{Pb}}$ and FCal $\sum E_{\text{T}}^{\text{Pb}}$ as a function of x_p

Distributions of normalized $E_{\text{ZDC}}^{\text{Pb}}$ and FCal $\sum E_{\text{T}}^{\text{Pb}}$ in dijet events are presented in intervals of x_p, the estimated Bjorken-x in the proton. The results for $E_{\text{ZDC}}^{\text{Pb}}$ are displayed in Figure 5.
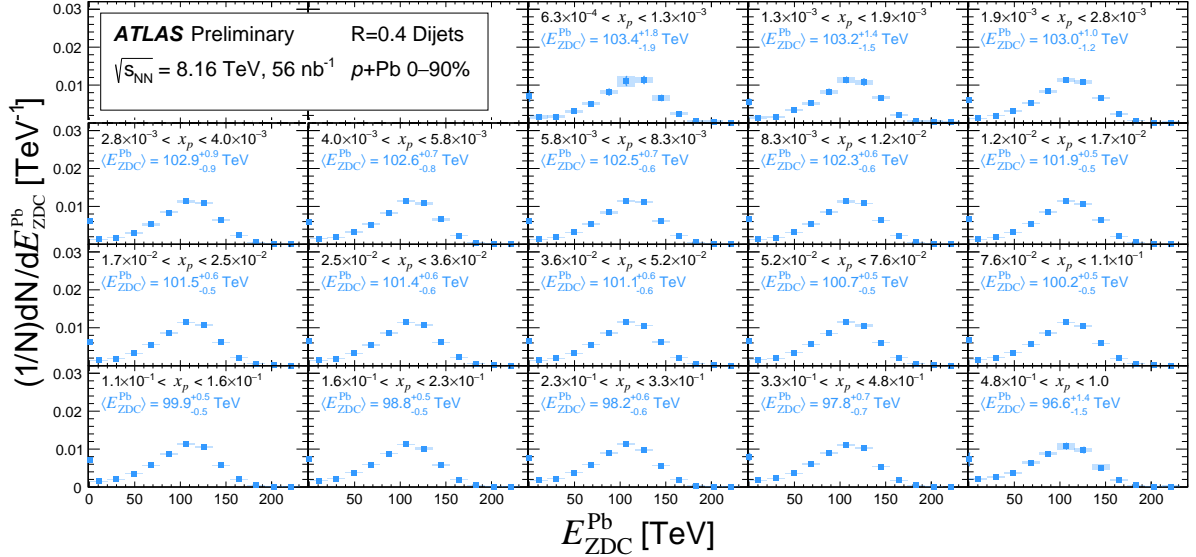

Figure 5: Normalized Pb-going ZDC energy spectrum. Each panel represents an x_p selection in dijet events. In each bin of x_p, the $\langle E_{\text{ZDC}}^{\text{Pb}} \rangle$ with uncertainties (in units of TeV) is displayed in blue text. The horizontal and vertical shaded areas represent the bin width and systematic uncertainty, respectively. The black vertical error bars represent the statistical uncertainty.

It is relevant to point out that the first bin in all the panels of Figure 5 (and in Figure 7) is set to 0–1 TeV, to isolate events that are compatible with zero neutrons in the detector. A shift toward lower values of the mean of the ZDC energy distribution can be observed with increasing x_p. The distribution of FCal $\sum E_{\text{T}}^{\text{Pb}}$ is presented, in the same fashion, in Figure 6.

To further analyze the shift of the energy deposited in the ZDC towards lower energies with increasing values of x_p, Figure 7 shows a comparison of $E_{\text{ZDC}}^{\text{Pb}}$ distributions in well-separated bins of x_p. The bottom panel of Figure 7 shows the ratio of the intermediate and high-x_p $E_{\text{ZDC}}^{\text{Pb}}$ distributions to that in low-x_p dijet events. The negative slope of these ratios indicates that, relative to a lower-x_p selection, higher-x_p events have a $E_{\text{ZDC}}^{\text{Pb}}$ distribution that is shifted towards lower energies.

Similarly, Figure 8 shows a comparison of FCal $\sum E_{\text{T}}^{\text{Pb}}$ distributions in three distinct bins of x_p. The distributions display a significant shift toward lower values of FCal $\sum E_{\text{T}}^{\text{Pb}}$ with x_p, as one would expect from the results presented by ATLAS in [16], where in high-x_p selections a deficit (enhancement) of events with large (small) FCal $\sum E_{\text{T}}^{\text{Pb}}$ was observed via a suppression of the central-to-peripheral ratio, R_{CP}. The bottom panel of Figure 8 shows the ratio of the intermediate and high-x_p FCal $\sum E_{\text{T}}^{\text{Pb}}$ distributions to that in low-x_p dijet events. As in Figure 7, the negative slope observed in this bottom panel indicates a relative shift towards lower energies of the higher-x_p FCal $\sum E_{\text{T}}^{\text{Pb}}$ distributions, with respect to the lower-x_p
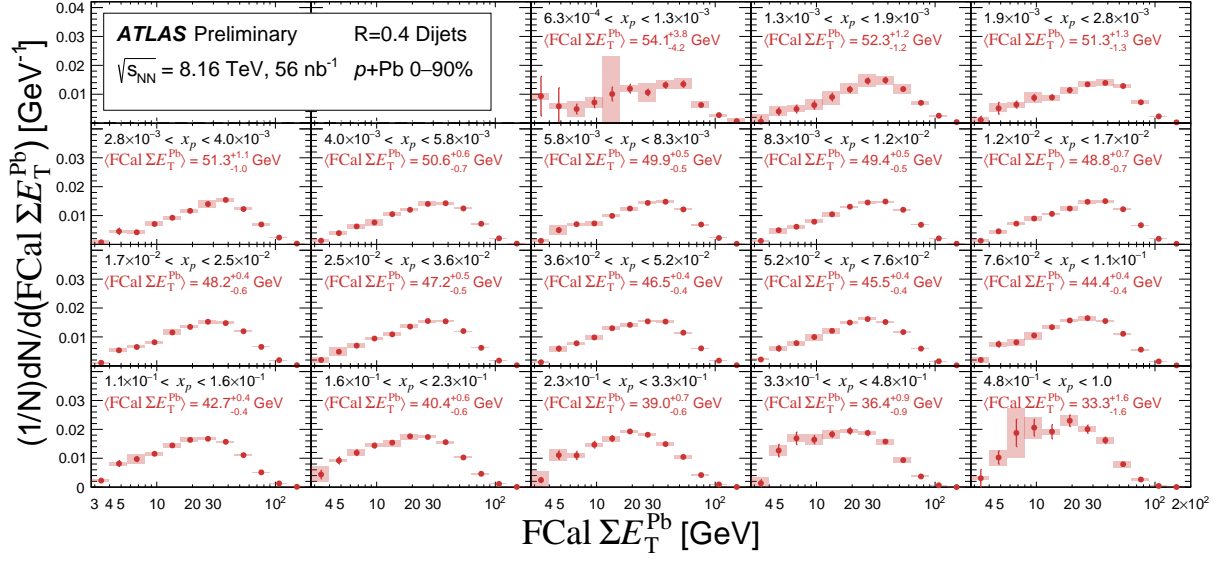
Figure 6: Normalized FCal $\sum E_T^{Pb}$ spectrum. Each panel represents an x_p selection in dijet events. In each bin of x_p, the $\langle$FCal $\sum E_T^{Pb}\rangle$ with uncertainties (in units of TeV) is displayed in red text. The horizontal and vertical shaded areas represent the bin width and systematic uncertainty, respectively. The black vertical error bars represent the statistical uncertainty.

distribution. The magnitude of this shift is visibly larger in the FCal $\sum E_T^{Pb}$ case compared to the E_{ZDC}^{Pb} case.
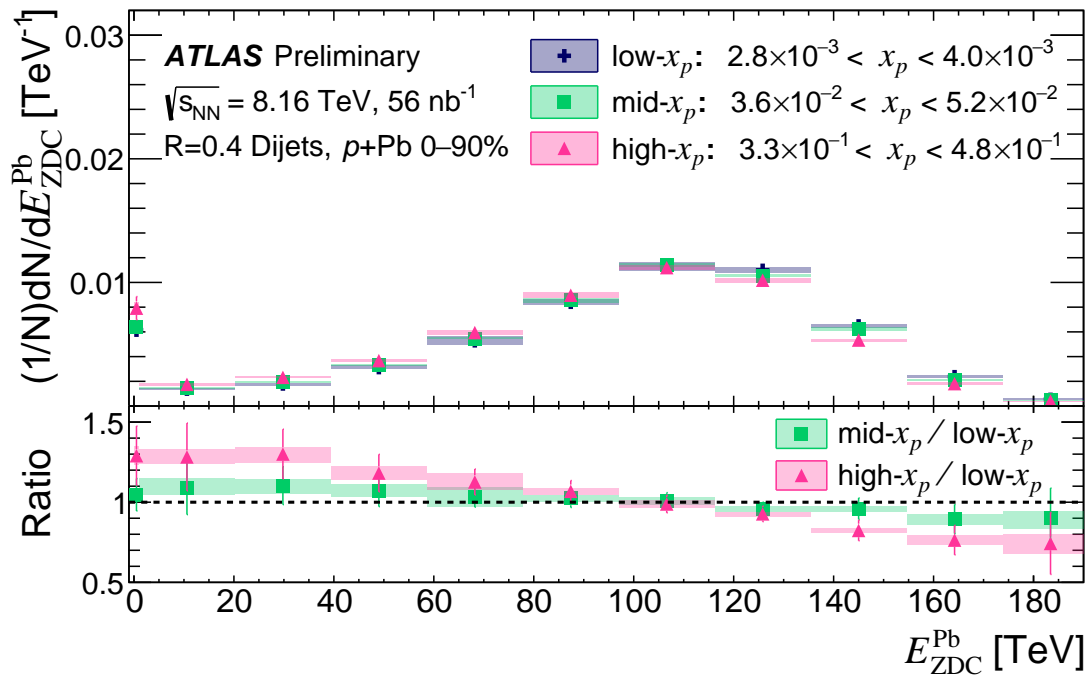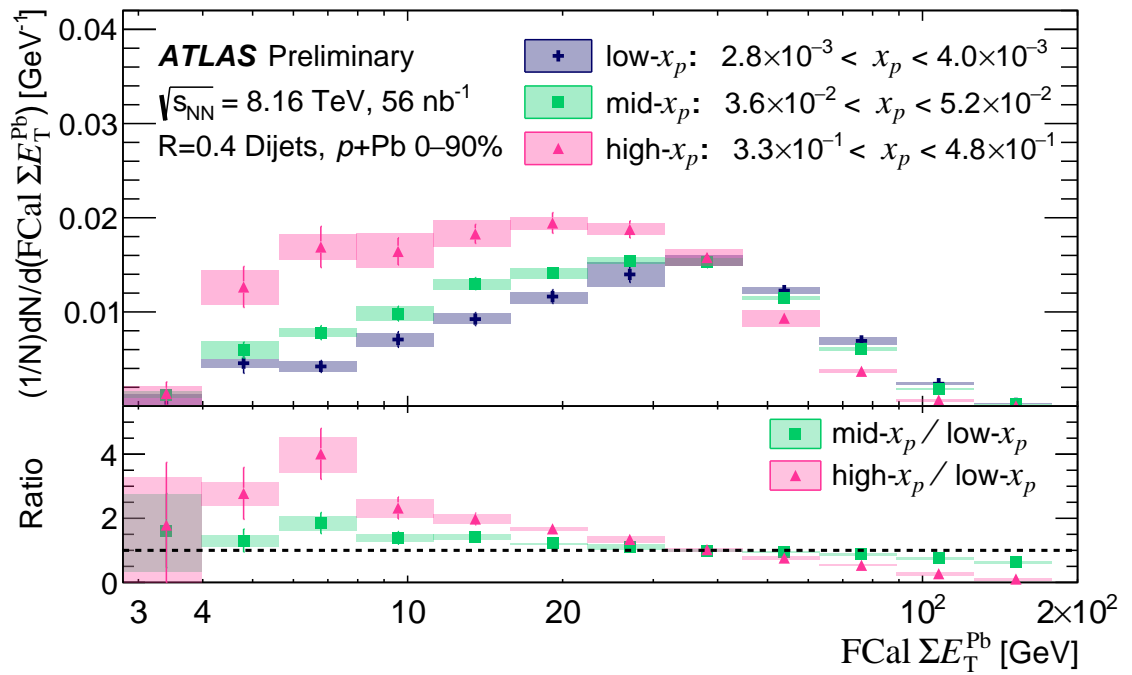
Figure 7: $E_{\mathrm{ZDC}}^{\mathrm{Pb}}$ distributions plotted for three selections of x_p: a low, moderate, and high selection. Each distribution is normalized in order to display the change of the $E_{\mathrm{ZDC}}^{\mathrm{Pb}}$ distribution shape with x_p. The bottom plot displays the ratio between the moderate and high-x_p selection over the low-x_p selection. Energy below the ZDC detection threshold (e.g. formally assigned as zero by ZDC reconstruction) is reported in a dedicated bin.

Figure 8: FCal $\sum E_T^{Pb}$ distributions plotted for three selections of x_p: a low, moderate, and high selection. These distributions are normalized in order to display the change of the FCal $\sum E_T^{Pb}$ distribution shape with x_p. The bottom plot displays the ratio between the moderate and high-x_p selection over the low-x_p selection.
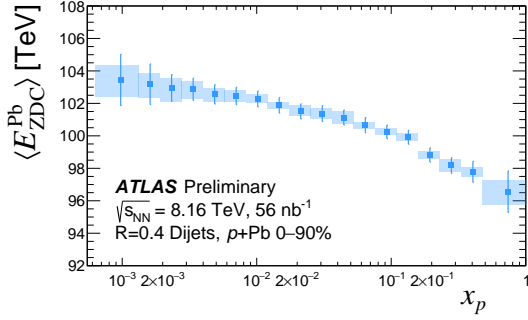
Figure 9: $\langle E_{\mathrm{ZDC}}^{\mathrm{Pb}} \rangle$ reported as a function of x_p. The horizontal and vertical shaded areas represent the bin width and systematic uncertainty, respectively. The vertical error bars represent the statistical uncertainty.
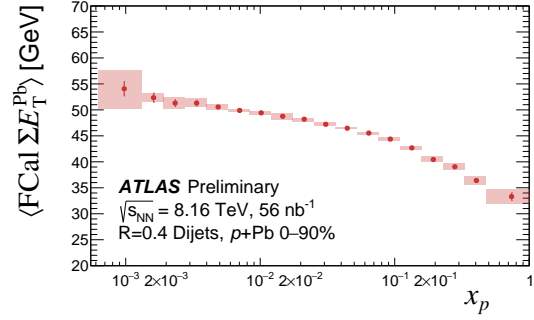
Figure 10: $\langle \mathrm{FCal} \sum E_{\mathrm{T}}^{\mathrm{Pb}} \rangle$ as a function of x_p. The horizontal and vertical shaded areas represent the bin width and systematic uncertainty, respectively. The vertical error bars represent the statistical uncertainty.

To better understand the correlations between x_p and the energy (transverse energy) detected in the ZDC (FCal), the averages of the distributions are presented in Figures 9 and 10 for the ZDC and FCal, respectively. One can notice how both distributions tend to decrease as a function of x_p, in particular in the region $x_p \gtrsim 2 \cdot 10^{-2}$, corresponding to the onset of effects attributed to small proton size configurations in [16]. The energy accumulated in the Pb-going side of the ZDC decreases by up to ~5% in this region, while an up to 40% decrease is observed for the FCal. When considering the statistical and systematic uncertainties on the highest x_p bin, the measurement of $\langle E_{\mathrm{ZDC}}^{\mathrm{Pb}} \rangle$ is more than 3 standard deviations away from the nominal value of $\langle E_{\mathrm{ZDC}}^{\mathrm{Pb}} \rangle$ in the bin centered around $x_p \approx 2 \cdot 10^{-2}$. Interestingly, the observed decrease of ~5% in the $\langle E_{\mathrm{ZDC}}^{\mathrm{Pb}} \rangle$ corresponds to, on average, an energy detected in the ZDC characteristic of two less beam energy neutrons.

Figure 11 shows the comparison between $E_{\mathrm{ZDC}}^{\mathrm{Pb}}$ and $\mathrm{FCal} \sum E_{\mathrm{T}}^{\mathrm{Pb}}$, both normalized to their maximum. The lower panel shows the ratio of the relative change in $\langle \mathrm{FCal} \sum E_{\mathrm{T}}^{\mathrm{Pb}} \rangle$ over the relative change in $\langle E_{\mathrm{ZDC}}^{\mathrm{Pb}} \rangle$ as a function of x_p. For x_p bins $\lesssim 2 \cdot 10^{-2}$ the relative change in $\langle E_{\mathrm{ZDC}}^{\mathrm{Pb}} \rangle$ is $\ll 1$ and the ratio becomes poorly defined, as one can observe by the large error bars. However, for the region $x_p \gtrsim 2 \cdot 10^{-2}$ the ratio is rather stable around a constant value, as demonstrated by the fit displayed in the figure. This result shows how, compared to the transverse energy at forward rapidities, the energy deposited in the ZDC in p+Pb collisions is about 6 times less sensitive to the hard process kinematics.
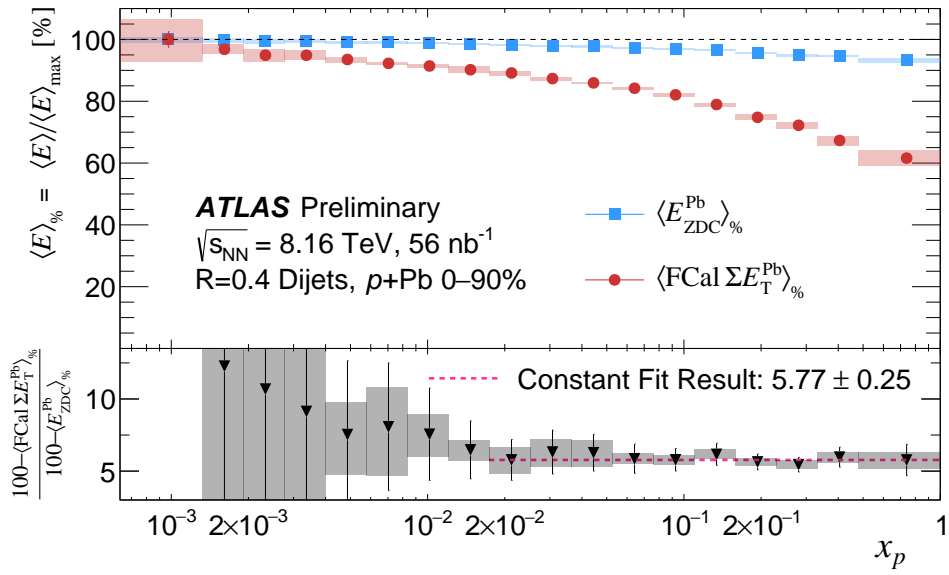
Figure 11: $\langle E_{\mathrm{ZDC}}^{\mathrm{Pb}} \rangle$ as a function of x_p (blue) compared to $\langle \mathrm{FCal} \sum E_{\mathrm{T}}^{\mathrm{Pb}} \rangle$ as a function of x_p (red). Both plots are normalized to their maximum value, in order to display both quantities on the same scale. The bottom plot shows the ratio of the relative change in $\langle \mathrm{FCal} \sum E_{\mathrm{T}}^{\mathrm{Pb}} \rangle$ over the relative change in $\langle E_{\mathrm{ZDC}}^{\mathrm{Pb}} \rangle$. The horizontal and vertical shaded areas represent the bin width and systematic uncertainty, respectively.

6.2 Correlation between $E_{\text{ZDC}}^{\text{Pb}}$ and FCal $\sum E_{\text{T}}^{\text{Pb}}$

The correlation between the transverse energy produced by the interactions of the participants (FCal $\sum E_{\text{T}}^{\text{Pb}}$) and the energy deposited by the spectator neutrons in the ZDC ($E_{\text{ZDC}}^{\text{Pb}}$) in x_p selections, measured at the reconstructed level, was also studied. The distributions in each x_p selection are shown in Figure 12. The Pearson correlation coefficient ($r_{E_{\text{ZDC}}^{\text{Pb}},\text{FCal}\sum E_{\text{T}}^{\text{Pb}}}$), calculated using Equation 2, between $E_{\text{ZDC}}^{\text{Pb}}$ and FCal $\sum E_{\text{T}}^{\text{Pb}}$ as a function of x_p is reported in Figure 13. A positive value for $r_{E_{\text{ZDC}}^{\text{Pb}},\text{FCal}\sum E_{\text{T}}^{\text{Pb}}}$ indicates that a positive correlation exists between FCal $\sum E_{\text{T}}^{\text{Pb}}$ and $E_{\text{ZDC}}^{\text{Pb}}$ across all x_p selections. A small decrease in the Pearson correlation coefficient is observed with increasing x_p, particularly in the region $x_p \gtrsim 5 \cdot 10^{-2}$, corresponding to the onset of effects attributed to CFs in [16]. This finding suggests that, in a smaller proton configuration, the forward transverse energy produced by the interactions of the participants is slightly less correlated with the number of spectator neutrons at very forward rapidities.

$$r_{x,y} = \frac{\sum_{i=1}^{n} (x_i - \bar{x})(y_i - \bar{y})}{\sqrt{\sum_{i=1}^{n} (x_i - \bar{x})^2}\sqrt{\sum_{i=1}^{n} (y_i - \bar{y})^2}} \tag{2}$$

To further study the evolution of the correlation between FCal $\sum E_{\text{T}}^{\text{Pb}}$ and $E_{\text{ZDC}}^{\text{Pb}}$ with x_p, Figure 14 reports $\langle \text{FCal} \sum E_{\text{T}}^{\text{Pb}} \rangle$ as a function of $E_{\text{ZDC}}^{\text{Pb}}$ in different x_p bins. A striking linearity of $\langle \text{FCal} \sum E_{\text{T}}^{\text{Pb}} \rangle$ as a function of $E_{\text{ZDC}}^{\text{Pb}}$ is observed in the range 0–155 TeV in $E_{\text{ZDC}}^{\text{Pb}}$ for all the x_p bins. In Figure 14, each distribution is fitted to a linear function ($f(x) = m \cdot x + b$) over that domain to capture the underlying relation between the energies measured in the two calorimeters. The data above 155 TeV are not considered in the fit since visible saturation effects start to appear. This behavior is likely due to fluctuations in the nuclear break-up occurring in events characterized by the highest (most central) event activity (collision geometry). The dependence of the linear fit's slope and intercept on the fit range was studied by systematically varying the upper limit of the fit range to cover ±1 bin in $E_{\text{ZDC}}^{\text{Pb}}$ with respect to the nominal choice of 155 TeV. Figure 15 overlays results from Figure 14 for three x_p selections. The slope of the linear correlation between $\langle \text{FCal} \sum E_{\text{T}}^{\text{Pb}} \rangle$ and $E_{\text{ZDC}}^{\text{Pb}}$ decreases progressively moving from low to high-x_p values.

The evolution of the linear fit's slope, which is proportional to the 'per neutron FCal energy', as a function of x_p is reported in Figure 16. This quantity is a useful metric for quantifying how the relationship between $E_{\text{ZDC}}^{\text{Pb}}$ and FCal $\sum E_{\text{T}}^{\text{Pb}}$ changes with x_p. However, it is important to note that a change in the number of neutrons does not directly imply a change in the transverse energy produced by the interactions of the participants at forward rapidity. A consistent x_p-driven reduction of the 'per neutron FCal energy' is observed in the study of jet yield modifications over the same x_p range [16]. The intercept terms of the linear fits, which represent the 'FCal energy at zero neutrons', are shown as a function of x_p in Figure 17. A slight decrease of FCal $\sum E_{\text{T}}^{\text{Pb}}$ at zero neutrons is observed in high-x_p events; however, this quantity may be biased by the centrality cut applied on FCal $\sum E_{\text{T}}^{\text{Pb}}$ to reject UPC contributions. Both the 'per neutron FCal energy' and the 'FCal energy at zero neutrons' are only modestly affected by systematic uncertainties due to the fit range selection.
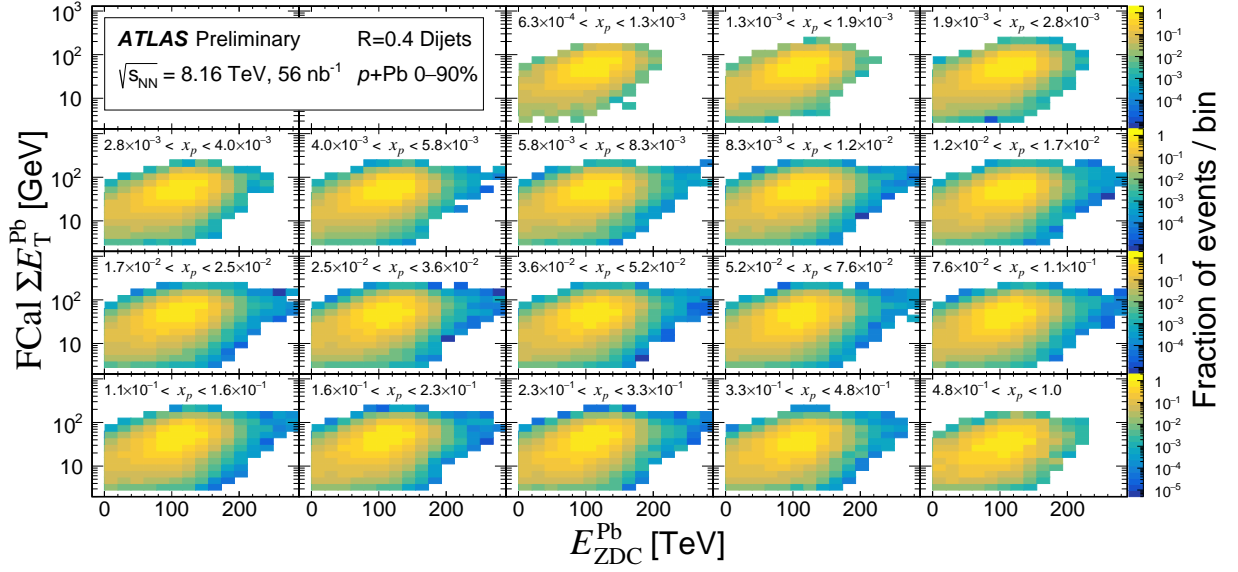
Figure 12: Correlation plot between $E_{\mathrm{ZDC}}^{\mathrm{Pb}}$ and FCal $\sum E_{\mathrm{T}}^{\mathrm{Pb}}$. Each panel represents an x_p selection made at the reconstructed level, where x_p is determined starting from the kinematics of the dijet events. The 0-1 TeV bin in $E_{\mathrm{ZDC}}^{\mathrm{Pb}}$ is still present, but is barely visible in the scale of this plot.
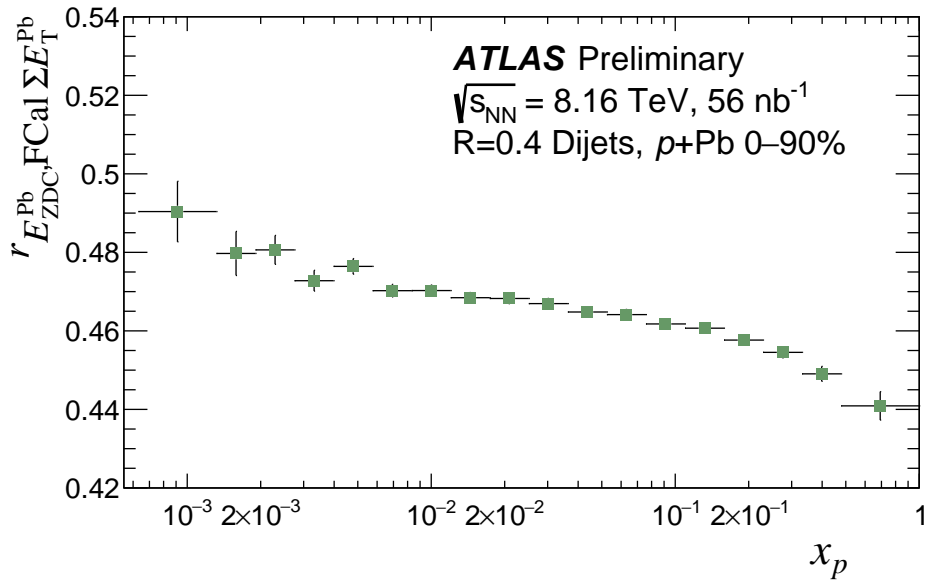

Figure 13: Sample Pearson correlation coefficient ($r_{E_{\mathrm{ZDC}}^{\mathrm{Pb}}, \mathrm{FCal} \sum E_{\mathrm{T}}^{\mathrm{Pb}}}$) between $E_{\mathrm{ZDC}}^{\mathrm{Pb}}$ and FCal $\sum E_{\mathrm{T}}^{\mathrm{Pb}}$, analyzed as a function of x_p. Horizontal error bars represent the bin widths, while vertical error bars represent the standard error associated to $r_{E_{\mathrm{ZDC}}^{\mathrm{Pb}}, \mathrm{FCal} \sum E_{\mathrm{T}}^{\mathrm{Pb}}}$.
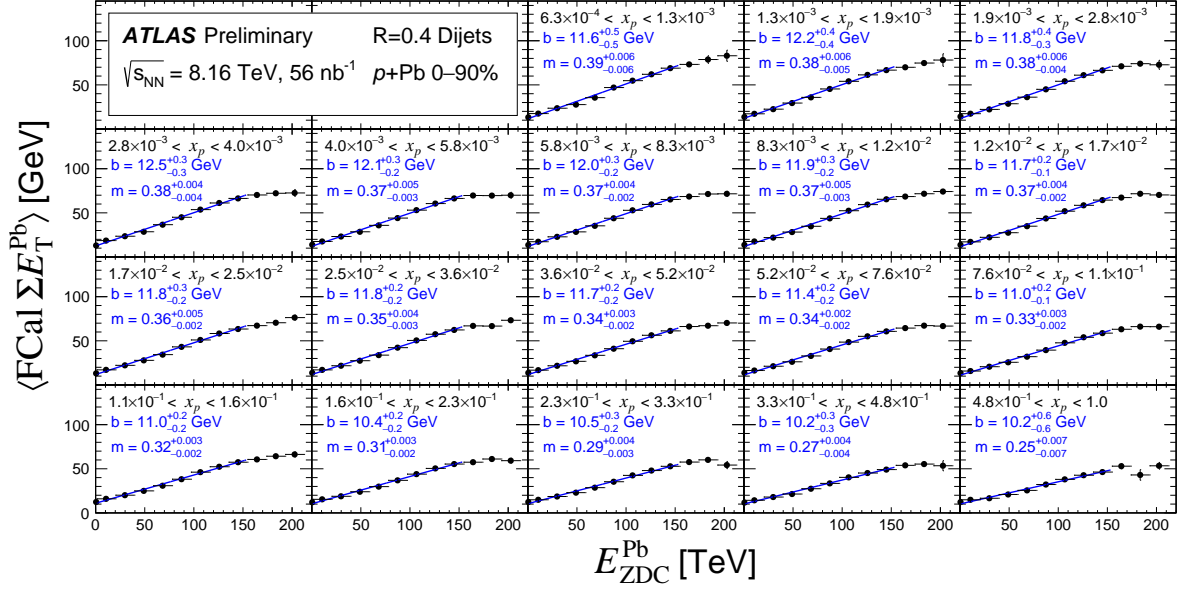
Figure 14: $\langle \text{FCal} \sum E_{\text{T}}^{\text{Pb}} \rangle$ reported as a function of $E_{\text{ZDC}}^{\text{Pb}}$. Each panel represents an x_p selection made at the reconstructed level, where x_p is determined starting from the kinematics of the dijet events. The values of $\langle \text{FCal} \sum E_{\text{T}}^{\text{Pb}} \rangle$ as a function of $E_{\text{ZDC}}^{\text{Pb}}$ are fit to linear functions of the form $f(x) = m \cdot x + b$. The slope and intercept of each fit are reported in their respective panels.
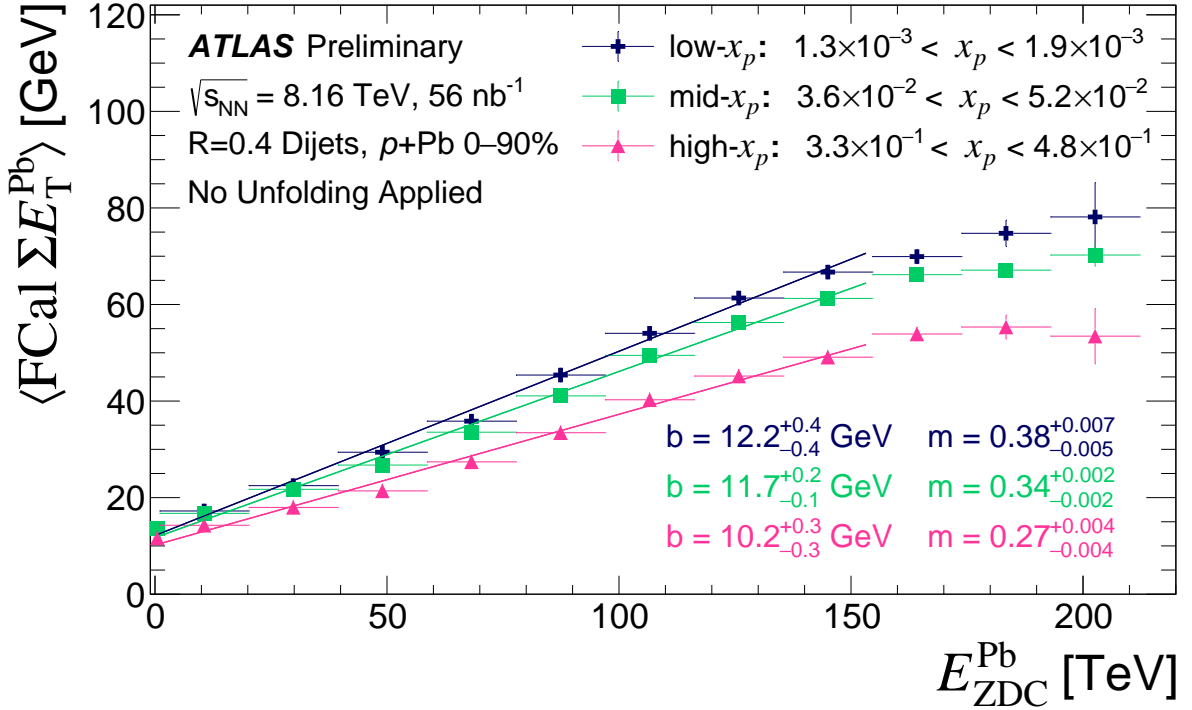

Figure 15: $\langle \text{FCal} \sum E_{\text{T}}^{\text{Pb}} \rangle$ plotted as a function of $E_{\text{ZDC}}^{\text{Pb}}$ for three selections of x_p: a low, moderate, and high selection. The data in each bin are fit to a linear form ($f(x) = m \cdot x + b$) with fit parameters (and fit uncertainties) reported on the figure.
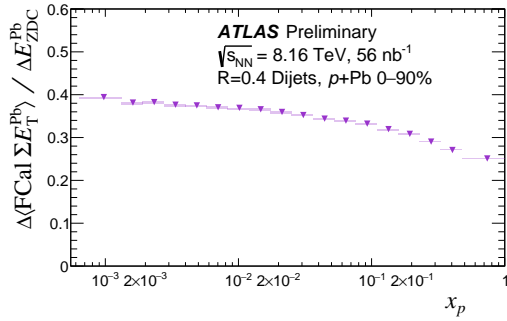
18

Figure 16: Slope of linear fits to $\langle \text{FCal} \sum E_{\text{T}}^{\text{Pb}} \rangle$ vs $E_{\text{ZDC}}^{\text{Pb}}$ reported as a function of x_p. Error bars represent the uncertainties on the fit parameters (contained in the marker size). The shaded boxes represent the systematic dependence on the fit range.
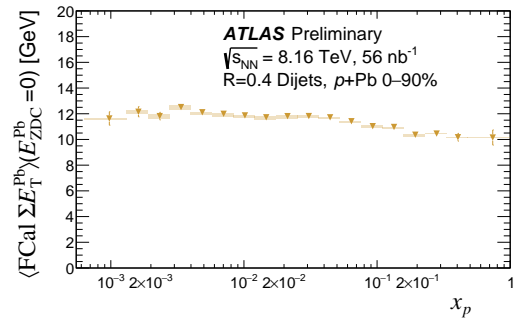
Figure 17: Intercept term of linear fits to $\langle \text{FCal} \sum E_{\text{T}}^{\text{Pb}} \rangle$ vs $E_{\text{ZDC}}^{\text{Pb}}$ reported as a function of x_p. Error bars represent the uncertainties on the fit parameters. The shaded boxes represent the systematic dependence on the fit range.

7 Conclusion

This note presents the first characterization of forward energy deposited in the ATLAS Forward Calorimeter and Zero-Degree Calorimeter in p+Pb collisions at $\sqrt{s_{\text{NN}}}$ = 8.16 TeV as a function of the estimated Bjorken-x of the proton, x_p, accessed in dijet events. Both $E_{\text{ZDC}}^{\text{Pb}}$ and FCal $\sum E_{\text{T}}^{\text{Pb}}$ are shown to be sensitive to x_p, especially in the region $x_p \gtrsim 2 \cdot 10^{-2}$, where previous ATLAS results from the same dataset [16] have shown strong evidence of event activity biases that can be linked to color fluctuation effects related to the proton configuration [12]. Further studies on the correlation between the two physics quantities as a function of x_p are also reported. In this case, the correlation is studied without unfolding of the experimental effects. The analysis of the 'per neutron FCal energy' and the 'FCal energy at zero neutrons' unveiled correlations that change with x_p, which can be used to advance the modeling of event activity and nuclear breakup in p+Pb collisions characterized by the presence of a hard-scattering.

References

[1] J. J. Ethier and E. R. Nocera, *Parton Distributions in Nucleons and Nuclei*,
Ann. Rev. Nucl. Part. Sci. **70** (2020) 43, arXiv: 2001.07722 [hep-ph] (cit. on p. 2).

[2] CMS Collaboration, *Study of W boson production in pPb collisions at $\sqrt{s_{NN}} = 5.02\,TeV$*,
Phys. Lett. B **750** (2015) 565, arXiv: 1503.05825 [hep-ex] (cit. on p. 2).

[3] ATLAS Collaboration,
Z boson production in p + Pb collisions at $\sqrt{s_{NN}} = 5.02\,TeV$ measured with the ATLAS detector,
Phys. Rev. C **92** (2015) 044915, arXiv: 1507.06232 [hep-ex] (cit. on p. 2).

[4] CMS Collaboration, *Studies of dijet transverse momentum balance and pseudorapidity distributions
in pPb collisions at $\sqrt{s_{NN}} = 5.02\,TeV$*, Eur. Phys. J. C **74** (2014) 2951,
arXiv: 1401.4433 [hep-ex] (cit. on p. 2).

[5] ATLAS Collaboration, *Photo-nuclear jet production in ultra-peripheral Pb+Pb collisions at
$\sqrt{s_{NN}} = 5.02\,TeV$ with the ATLAS detector*, (2022),
URL: https://cds.cern.ch/record/2806461 (cit. on p. 2).

[6] ATLAS Collaboration, *Observation of $t\bar{t}$ production in the lepton+jets and dilepton channels in
p+Pb collisions at $\sqrt{s_{NN}} = 8.16\,TeV$ with the ATLAS detector*, (2024),
arXiv: 2405.05078 [nucl-ex] (cit. on p. 2).

[7] CMS Collaboration, *Observation of Top Quark Production in Proton–Nucleus Collisions*,
Phys. Rev. Lett. **119** (2017) 242001, arXiv: 1709.07411 [hep-ex] (cit. on p. 2).

[8] R. Aaij et al., *Study of prompt D^0 meson production in pPb collisions at $\sqrt{s_{NN}} = 5\,TeV$*,
JHEP **10** (2017) 090, arXiv: 1707.02750 [hep-ex] (cit. on p. 2).

[9] ATLAS Collaboration, *Dijet azimuthal correlations and conditional yields in pp and p+Pb
collisions at $\sqrt{s_{NN}} = 5.02\,TeV$ with the ATLAS detector*, Phys. Rev. C **100** (2019) 034903,
arXiv: 1901.10440 [nucl-ex] (cit. on p. 2).

[10] ATLAS Collaboration, *Centrality and rapidity dependence of inclusive jet production in
$\sqrt{s_{NN}} = 5.02\,TeV$ proton-lead collisions with the ATLAS detector*, Phys. Lett. B **748** (2015) 392,
arXiv: 1412.4092 [hep-ex] (cit. on pp. 2, 3).

[11] PHENIX Collaboration, *Centrality-dependent modification of jet-production rates in deuteron-gold
collisions at $\sqrt{s_{NN}} = 200\,GeV$*, Phys. Rev. Lett. **116** (2016) 122301,
arXiv: 1509.04657 [nucl-ex] (cit. on p. 2).

[12] M. Alvioli, L. Frankfurt, D. Perepelitsa and M. Strikman, *Global analysis of color fluctuation
effects in proton– and deuteron–nucleus collisions at RHIC and the LHC*,
Phys. Rev. D **98** (2018) 071502, arXiv: 1709.04993 [hep-ph] (cit. on pp. 2, 20).

[13] A. Mueller, 'Proc. XVII Rencontre de Moriond', 1982 (cit. on p. 2).

[14] S. Brodsky, 'Proc. XIII Intern. Syrup. on Multiparticle dynamics', Volendam, 1982 (cit. on p. 2).

[15] G. Bertsch, S. J. Brodsky, A. S. Goldhaber and J. G. Gunion,
Diffractive Excitation in Quantum Chromodynamics, Phys. Rev. Lett. **47** (5 1981) 297 (cit. on p. 2).

[16] ATLAS Collaboration, *Measurement of the centrality dependence of the dijet yield in p+Pb
collisions at $\sqrt{s_{NN}} = 8.16\,TeV$ with the ATLAS Detector*, Phys. Rev. Lett. **132** (2024) 102301,
arXiv: 2309.00033 [nucl-ex] (cit. on pp. 2, 3, 5–7, 10, 14, 16, 20).

[17] D. V. Perepelitsa,
Contribution to differential π0 and γdir modification in small systems from color fluctuation effects,
Phys. Rev. C **110** (2024) L011901, arXiv: 2404.17660 [nucl-th] (cit. on p. 2).

[18] ALICE Collaboration,
Centrality dependence of particle production in p-Pb collisions at $\sqrt{s_{NN}}$ = 5.02 TeV,
Phys. Rev. C **91** (2015) 064905, arXiv: 1412.6828 [nucl-ex] (cit. on p. 2).

[19] ATLAS Collaboration, *Strong constraints on jet quenching in centrality-dependent p+Pb collisions at 5.02 TeV from ATLAS*, Phys. Rev. Lett. **131** (2023) 072301, arXiv: 2206.01138 [nucl-ex] (cit. on pp. 2, 3, 6).

[20] ALICE Collaboration, *Study of very forward energy and its correlation with particle production at midrapidity in pp and p-Pb collisions at the LHC*, JHEP **08** (2022) 086, arXiv: 2107.10757 [nucl-ex] (cit. on p. 2).

[21] M. Alvioli, V. Guzey and M. Strikman,
Slicing Pomerons in ultraperipheral collisions using forward neutrons from nuclear breakup,
Phys. Rev. C **110** (2024) 025205, arXiv: 2402.19060 [hep-ph] (cit. on p. 2).

[22] L. Zheng, E. C. Aschenauer and J. H. Lee,
Determination of electron-nucleus collision geometry with forward neutrons,
Eur. Phys. J. A **50** (2014) 189, arXiv: 1407.8055 [hep-ex] (cit. on p. 3).

[23] ATLAS Collaboration, *The ATLAS Experiment at the CERN Large Hadron Collider*,
JINST **3** (2008) S08003 (cit. on pp. 3, 4).

[24] ATLAS Collaboration, *The ATLAS Collaboration Software and Firmware*,
ATL-SOFT-PUB-2021-001, 2021, URL: https://cds.cern.ch/record/2767187 (cit. on p. 3).

[25] ATLAS Collaboration, *ATLAS Insertable B-Layer: Technical Design Report*,
ATLAS-TDR-19; CERN-LHCC-2010-013, 2010,
URL: https://cds.cern.ch/record/1291633 (cit. on p. 4),
Addendum: ATLAS-TDR-19-ADD-1; CERN-LHCC-2012-009, 2012, URL:
https://cds.cern.ch/record/1451888.

[26] ATLAS Collaboration, *Production and integration of the ATLAS Insertable B-Layer*,
JINST **13** (2018) T05008, arXiv: 1803.00844 [physics.ins-det] (cit. on p. 4).

[27] ATLAS Collaboration, *Operation of the ATLAS trigger system in Run 2*, JINST **15** (2020) P10004,
arXiv: 2007.12539 [hep-ex] (cit. on p. 4).

[28] O. Adriani et al., *Study of forward physics in $\sqrt{s_{NN}}$ = 8.1 TeV proton-Lead ion collisions with the LHCf detector at the LHC*, tech. rep., CERN, 2016,
URL: https://cds.cern.ch/record/2135330 (cit. on p. 4).

[29] ATLAS Collaboration, *Measurement of the centrality dependence of the charged-particle pseudorapidity distribution in proton–lead collisions at $\sqrt{s_{NN}}$ = 5.02 TeV with the ATLAS detector*,
Eur. Phys. J. C **76** (2016) 199, arXiv: 1508.00848 [hep-ex] (cit. on p. 5).

[30] ATLAS Collaboration, *Transverse momentum and process dependent azimuthal anisotropies in $\sqrt{s_{NN}}$ = 8.16 TeV p+Pb collisions with the ATLAS detector*, Eur. Phys. J. C **80** (2020) 73,
arXiv: 1910.13978 [nucl-ex] (cit. on p. 5).

[31] GEANT4 Collaboration, S. Agostinelli et al., *GEANT4 – a simulation toolkit*,
Nucl. Instrum. Meth. A **506** (2003) 250 (cit. on p. 5).

[32] ATLAS Collaboration, *The ATLAS Simulation Infrastructure*, Eur. Phys. J. C **70** (2010) 823, arXiv: 1005.4568 [physics.ins-det] (cit. on p. 5).

[33] T. Sjöstrand et al., *An introduction to PYTHIA 8.2*, Comput. Phys. Commun. **191** (2015) 159, arXiv: 1410.3012 [hep-ph] (cit. on p. 5).

[34] ATLAS Collaboration, *ATLAS Pythia 8 tunes to 7 TeV data*, (2014), URL: https://cds.cern.ch/record/1966419 (cit. on p. 5).

[35] R. D. Ball et al., *Parton distributions with LHC data*, Nucl. Phys. B **867** (2013) 244, arXiv: 1207.1303 [hep-ph] (cit. on p. 5).

[36] ATLAS Collaboration, *Performance of the ATLAS Level-1 topological trigger in Run 2*, Eur. Phys. J. C **82** (2021) 7, arXiv: 2105.01416 [hep-ex] (cit. on p. 5).

[37] ATLAS Collaboration, *Measurements of the suppression and correlations of dijets in Pb+Pb collisions at $\sqrt{s_{NN}}$ = 5.02 TeV*, Phys. Rev. C **107** (5 2023) 054908, arXiv: 2205.00682 [nucl-ex] (cit. on p. 6).

[38] M. Cacciari, G. P. Salam and G. Soyez, *The anti-k_t jet clustering algorithm*, JHEP **04** (2008) 063, arXiv: 0802.1189 [hep-ph] (cit. on p. 6).

[39] G. D'Agostini, *A multidimensional unfolding method based on Bayes' theorem*, Nucl. Instrum. Meth. A **362** (1995) 487, ISSN: 0168-9002 (cit. on p. 7).

[40] T. Adye, 'Unfolding algorithms and tests using RooUnfold', *Proceedings, 2011 Workshop on Statistical Issues Related to Discovery Claims in Search Experiments and Unfolding (PHYSTAT 2011)* (CERN, Geneva, Switzerland, 17th–20th Jan. 2011) 313, arXiv: 1105.1160 [physics.data-an] (cit. on p. 7).

[41] ATLAS Collaboration, *Evaluating statistical uncertainties and correlations using the bootstrap method*, ATL-PHYS-PUB-2021-011, 2021, URL: https://cds.cern.ch/record/2759945 (cit. on p. 7).

[42] ATLAS Collaboration, *Jet energy scale and resolution measured in proton–proton collisions at $\sqrt{s}$ = 13 TeV with the ATLAS detector*, Eur. Phys. J. C **81** (2020) 689, arXiv: 2007.02645 [hep-ex] (cit. on p. 7).

[43] ATLAS Collaboration, *Jet energy scale and its uncertainty for jets reconstructed using the ATLAS heavy ion jet algorithm*, (2015), URL: https://cds.cern.ch/record/2008677 (cit. on p. 7).